*Bioinformatics*, 2025, **41(9)**, btaf451
https://doi.org/10.1093/bioinformatics/btaf451
Advance Access Publication Date: 11 August 2025
**Original Paper**

OXFORD

Gene expression

# Mitigation of multi-scale biases in cell-type deconvolution for spatially resolved transcriptomics using HarmoDecon

**Zirui Wang[1], Ke Xu[1], Yang Liu[1], Yu Xu[1], Lu Zhang[1,*]**

[1]Department of Computer Science, Hong Kong Baptist University, Kowloon Tong, Hong Kong, SAR

*Corresponding author. Department of Computer Science, Hong Kong Baptist University, Kowloon Tong, Hong Kong, SAR. E-mail: ericluzhang@hkbu.edu.hk.

Associate Editor: Anthony Mathelier

## Abstract

**Motivation:** The advent of spatially resolved transcriptomics (SRT) has revolutionized our understanding of tissue molecular microenvironments by enabling the study of gene expression in its spatial context. However, many SRT platforms lack single-cell resolution, necessitating cell-type deconvolution methods to estimate cell-type proportions in SRT spots. Despite advancements in existing tools, these methods have not addressed biases occurring at three scales: individual spots, entire tissue samples, and discrepancies between SRT and reference scRNA-seq datasets. These biases result in overbalanced cell-type proportions for each spot, mismatched cell-type fractions at the sample level, and data distribution shifts across platforms.

**Results:** To mitigate these biases, we introduce HarmoDecon, a novel semi-supervised deep learning model for spatial cell-type deconvolution. HarmoDecon leverages pseudo-spots derived from scRNA-seq data and uses Gaussian Mixture Graph Convolutional Networks to address the aforementioned issues. Through extensive simulations on multi-cell spots from STARmap and osmFISH, HarmoDecon outperformed 11 state-of-the-art methods. Additionally, when applied to legacy SRT platforms and 10x Visium datasets, HarmoDecon achieved the highest accuracy in spatial domain clustering and maintained strong correlations between cancer marker genes and cancer cells in human breast cancer samples. These results highlight the utility of HarmoDecon in advancing spatial transcriptomics analysis.

**Availability and implementation:** The HarmoDecon scripts, with the detailed tutorials, are available at https://github.com/ericcombiolab/HarmoDecon/tree/main.

## 1 Introduction

Spatially resolved transcriptomics (SRT) is a powerful technology that enables the exploration of gene expression profiles and the spatial landscape of corresponding transcripts. SRT has the potential to uncover the mechanism of cell-cell interactions (Shao *et al.* 2022, Li *et al.* 2023), elucidate tumor microenvironment (Hunter *et al.* 2021, Arora *et al.* 2023), monitor embryo development (Lohoff *et al.* 2022, Sampath Kumar *et al.* 2023), and explore the community structure of nerve (Close *et al.* 2021) and immune cells (Engblom *et al.* 2023). Nowadays, SRT data can be produced using imaging-based and sequencing-based platforms. Imaging-based SRT platforms are designed using *in situ* hybridization or fluorescence microscopy, such as STARmap (Wang *et al.* 2018b), seqFISH (Eng *et al.* 2019), osmFISH (Codeluppi *et al.* 2018), and MERFISH (Moffitt *et al.* 2018). They could provide gene expression with single-cell resolution and low dropout rates, but their performance is limited by the small numbers of cells and genes that can be captured.

Sequencing-based SRT platforms, including legacy ST (Ståhl *et al.* 2016), Slide-seq (Stickels *et al.* 2021), 10X Visium (10x Genomics 2020) and Stereo-seq (Chen *et al.* 2022a), utilize next-generation sequencing to capture whole transcriptomes across a large number of cells. However, these platforms come with a trade-off: each captured cell-like spatial unit (with a radius of 10–100 μm), known as a spot, may contain multiple cells. This fact leads to low spatial resolution at the cellular level, which substantially impacts the performance of downstream tasks, such as inferring cell-cell interactions (Shao *et al.* 2022, Li *et al.* 2023) and spatial domain clustering (Dong and Zhang 2022, Long *et al.* 2023). To increase the resolution of sequencing-based SRT techniques (referred to as SRT hereafter), cell-type deconvolution has been introduced to predict the cell-type proportion for each spot using single-cell RNA-seq (scRNA-seq) data from the same tissue. Numerous computational tools have been developed for cell-type deconvolution, which can be categorized into three types: matrix-based approaches, statistics-based approaches, and deep learning-based approaches. Matrix-based approaches utilize non-negative matrix factorization and non-negative least squares for cell-type deconvolution, such as SPOTlight (Elosua-Bayes *et al.* 2021), SpatialDWLS (Dong and Yuan 2021), CARD (Ma and Zhou 2022), and Redeconve (Zhou *et al.* 2023). Statistics-based approaches, including Stereoscope (Andersson *et al.* 2020), RCTD (Cable *et al.* 2022), and Cell2location (Kleshchevnikov *et al.* 2022), typically assume that the transcript read counts follow a Poisson distribution or a negative binomial distribution. They utilize linear models to predict the parameters of these two distributions by weighted aggregation of different cell type signatures. There is a growing trend in developing deep learning-based approaches that generate pseudo-spots using cells from

**Received:** 24 December 2024; **Revised:** 9 June 2025; **Editorial Decision:** 3 August 2025; **Accepted:** 8 August 2025

scRNA-seq or SRT platforms with single-cell resolution, such as DSTG (Song and Su 2021), Tangram (Biancalani *et al.* 2021), STdGCN (Li and Luo 2024), and SPACEL (Xu *et al.* 2023). Recent spatially informed cell-type deconvolution approaches, such as CARD and STdGCN, integrate spatial information to ensure that spots in close proximity have similar cell-type proportions.

While these cell-type deconvolution tools have been extensively used across various SRT platforms (Li *et al.* 2023, Vahid *et al.* 2023), our preliminary study has identified some unsolved biases. First, spots from most of the platforms are typically small and contain a limited number of cells. For example, in the 10x Genomics Visium platform, each spot has a diameter of 55 μm and generally captures between 1 and 10 cells (10x Genomics 2020). Many existing cell-type deconvolution methods for SRT are inherited from the ones designed for bulk RNA-seq data (Walker *et al.* 2020), which measures gene expression across hundreds of thousands of cells and may cover all the candidate cell types. These approaches ignore the fact that the cells from different candidate cell types are not evenly distributed for each spot of SRT.

We downloaded two SRT datasets with single-cell resolution [STARmap (Wang *et al.* 2018b) and osmFISH (Codeluppi *et al.* 2018)] and aggregated individual cells into multi-cell spots based on their spatial coordinates (see Section 2, Fig. 2a), with each simulated spot typically containing 1 to 10 cells (Fig. S1, available as supplementary data at *Bioinformatics* online). Our observations revealed that cells from different cell types were not uniformly distributed within these simulated multi-cell spots. Instead, there commonly exist dominant cell types, with some types absent in the spot, demonstrating a long-tailed distribution while visualizing their proportions ordered by abundance (Fig. 2a and b). In contrast, many existing methods, such as Cell2Location and SPACEL, tended to produce overbalanced cell-type proportions for each spot (Fig. S2, available as supplementary data at *Bioinformatics* online and Fig. 5).

Second, the bias from sample-wise cell-type fractions is often overlooked. As we know, similar to spots, each sample slice has its own cell-type fractions that reflect its characteristics. Existing approaches primarily focus on optimizing cell-type proportions at the spot level without ensuring that the predicted sample-wide cell-type fractions are consistent with expected values. In our analysis of simulated multi-cell spot datasets, we calculated the sample-level cell-type fractions by aggregating cell-type proportions across all spots and observed that the sample-level cell-type fractions estimated by existing tools, deviated significantly from the ground truth, especially for dominant cell types (Fig. 4b; Fig. S3, available as supplementary data at *Bioinformatics* online).

Third, a bias can also arise from the platform effect between SRT and scRNA-seq datasets. The platform effect has been documented in previous studies (Cable *et al.* 2022) and was also observed in our simulated multi-cell spots (Fig. S4, available as supplementary data at *Bioinformatics* online). This platform effect leads to shifts in gene expression values, complicating downstream analyses. While some statistics-based approaches, such as RCTD, have developed strategies to address this issue, deep learning-based methods have yet to tackle this challenge effectively.

In this study, we propose HarmoDecon (Fig. 1), a novel semi-supervised deep learning model designed to mitigate these multi-scale biases in SRT data deconvolution. We generated pseudo-spots with known cell-type proportions by aggregating

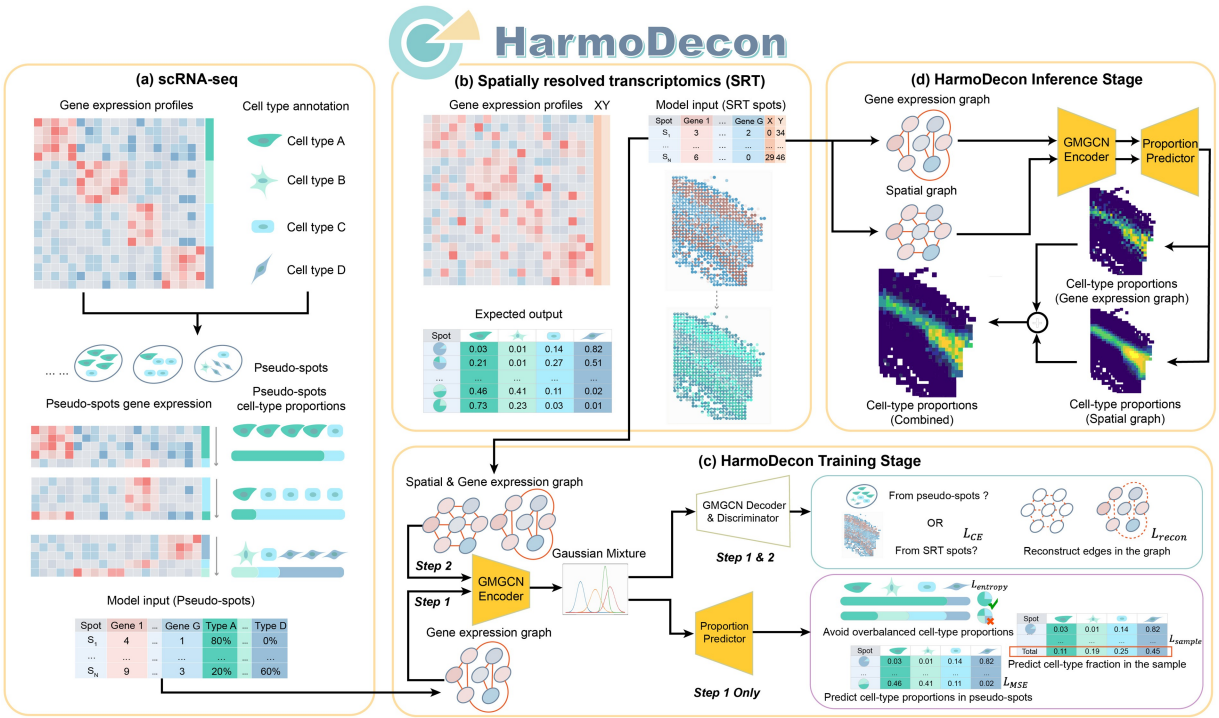


**Figure 1.** The workflow of HarmoDecon. HarmoDecon is designed for spatially informed cell-type deconvolution for SRT data. HarmoDecon requires (i) gene expression and cell-type annotations of single cells from scRNA-seq (a); (ii) gene expression and spatial coordinates of SRT spots (b); in the training stage, HarmoDecon generates pseudo-spots with known cell-type proportions by randomly selecting cells from scRNA-seq data (a). During the training stage, HarmoDecon incorporates GMGCN to accept spatial and gene expression graphs from SRT spots and gene expression graphs from pseudo-spots (c). After training, in the inference procedure, HarmoDecon combines predictions from both spatial and gene expression graphs to deliver highly accurate cell-type deconvolution results (d).

single cells from scRNA-seq data with annotated cell types (Section 2, Fig. 1a and b). HarmoDecon incorporates Gaussian Mixture Graph Convolutional Network (GMGCN) to capture the relationship between spots from three graphs (Section 2): (i) a gene expression similarity graph for pseudo-spots; (ii) a gene expression similarity graph for SRT spots; and (iii) a spatial proximity graph for SRT spots. To reduce existing biases, HarmoDecon utilizes (i) an entropy-based loss to avoid overbalanced cell-type distributions across spots, (ii) a sample-level loss function to ensure that the predicted cell-type fractions align with the expected proportions from the whole tissue, and (iii) a domain adaptation module (Ganin *et al.* 2016) to mitigate platform effect between SRT and scRNA-seq data (Section 2). Our extensive benchmarking on various datasets demonstrates that HarmoDecon outperforms 11 state-of-the-art deconvolution tools, offering significant improvements in both spot-level and sample-level predictions.

## 2 Materials and methods

### 2.1 Data preprocessing

We applied the same data preprocessing strategy to the datasets from SRT and matched scRNA-seq using Scanpy package (Wolf *et al.* 2018), including (i) library size normalization (*scanpy.pp.normalize_total*), (ii) logarithmic normalization on gene expression profiles (*scanpy.pp.log1p*), (iii) gene-wise z-score standardization on gene expression profiles (*scanpy.pp.scale*), (iv) highly variable genes shared in SRT and scRNA-seq (*scanpy.pp.highly_variable_genes*, with default thresholds).

### 2.2 Simulate multi-cell spots from STARmap and osmFISH

The landscape of the datasets from STARmap and osmFISH was split into quadrilateral grids with intervals of 750 and 800 pixels. Each single-cell resolution spot (with cell-type annotation) was assigned to its closest grid by computing its distance from grid centers (Chen *et al.* 2022b, Li *et al.* 2022). Each grid represented a simulated multi-cell spot with 1–16 cells (STARmap) and 1–19 cells (osmFISH). A total of 189 (STARmap) and 737 (osmFISH) multi-cell spots are simulated.

### 2.3 Generate pseudo-spots from scRNA-seq data

We used scRNA-seq data to generate pseudo-spots. For each pseudo-spot, we assumed that the number of involved cells ($n_c$) follows a Poisson distribution (with at least one cell per spot), and the number of involved cell types ($n_k$) follows a discrete uniform distribution.

$$n_c = Poisson(\lambda) + 1 \tag{1}$$
$$n_k \sim \mathbb{U}(1, N_K) \tag{2}$$

$\lambda$ ($\lambda = 5$) and $N_K$ ($N_K = 4$) represent the mean of the Poisson distribution and the maximum number of cell types allowed included in a pseudo-spot. The variable $n_c$ is modeled as a Poisson-distributed random variable with parameter $\lambda$, incremented by 1, to make sure the number of cells per spot is not zero. The Poisson distribution can effectively model such variability where events (cell counts) occur independently over a fixed space or time. And the discrete uniform distribution offers a simple and flexible framework for modeling scenarios where we assume an equal probability of observing various numbers of cell types across different spots. We compared our performance using Poisson and discrete uniform distributions with that of the normal distribution (having the same mean value and a standard deviation set to 1) (Fig. S22, available as supplementary data at *Bioinformatics* online). The results confirmed the effectiveness of our default settings compared to the normal distribution.

For pseudo-spot $i$, we randomly selected $n_c$ cells from $n_k$ cell types with equal probabilities and aggregated their gene raw counts to generate a gene expression profile (Fig. S21, available as supplementary data at *Bioinformatics* online). We sampled each cell type with equal probabilities, rather than adhering to the distribution of the reference scRNA-seq, due to inherent platform shifts between the reference scRNA-seq and SRT regarding cell types (Fig. S29, available as supplementary data at *Bioinformatics* online). Since the actual cell-type distributions in SRT are unknown, sampling from a uniform cell-type distribution is considered more robust.

After sampling cells, the expression value of a pseudo-spot $i$ is represented as $x_i$, which is the sum of all expression values of the selected single cells. The cell-type proportion for the pseudo-spot $i$ is represented as $y_i$, calculated by the number of each type of cell divided by the total number. In this study, we sampled 50 000 pseudo-spots for each experiment.

### 2.4 Construct spatial and gene expression graphs

During training, HarmoDecon accepts three kinds of graphs: (i) a spatial graph for SRT spots; (ii) a gene expression graph for SRT spots; and (iii) 250 gene expression graphs for pseudo-spots, with each containing 200 spots.

The spatial graph connects spots by selecting their top six mutual nearest neighbors based on the Euclidean distance of spots' spatial coordinates. The gene expression graphs are constructed by linking spots (pseudo-spots) to their top six mutual nearest neighbors based on the cosine similarities of their gene expression profiles. For pseudo-spots formed gene expression graphs, links of each graph are built internally within 200 spots.

### 2.5 Training and inference of HarmoDecon

HarmoDecon is based on the Gaussian Mixture Graph Convolutional Network (GMGCN), which learns representations of spots and pseudo-spots from spatial and gene expression graphs, respectively. For pseudo-spots, $A \in \mathbb{R}^{n\times n}$ is the adjacency matrix of the gene expression graph with gene expression profiles $X = [x_1, x_2, \ldots, x_n] \in \mathbb{R}^{n\times g}$ as node feature, where $n$ is the number of pseudo-spots in the graph. GMGCN could generate $Z = [z_1, z_2, \ldots, z_n] \in \mathbb{R}^{n\times 512}$ as pseudo-spot embeddings, where $z_i$ is sampled from $k$th component of Gaussian Mixture Model (with means $\mu_{ik}$ and variances $\sigma_{ik}$) in the latent space (Notes, available as supplementary data at *Bioinformatics* online). We have $q(z_i|X, A) = \mathcal{N}(z_{ik}; \tilde{\mu}_{ik}, \tilde{\sigma}_{ik}{}^2 I)$, $z_i = \tilde{\mu}_{ik} + \tilde{\sigma}_{ik}{}^{\circ}\varepsilon$, where $\varepsilon \sim \mathcal{N}(0, I)$.

We define the reconstruction loss function as:

$$L_{\text{recon}}(A, Z) = -\sum_{i=1}^{n}\sum_{j=1}^{n}\Big[A_{ij}\log\Big(\text{sigmoid}(z_i^T z_j)\Big) + (1 - A_{ij})\log\Big(1 - \text{sigmoid}(z_i^T z_j)\Big)\Big] \tag{3}$$

$z_i$ is further passed to a two-layer Multilayer Perceptron (Notes, available as supplementary data at *Bioinformatics* online) to predict the cell-type proportion of pseudo-spot $i$ ($f_\theta : \mathbf{z}_i \to \tilde{y}_i \in \mathbb{R}^{CT}$), where $CT$ were the number of cells and

cell types. We also introduced mean squared error (MSE) loss to minimize the observed and predicted cell-type proportions.

$$L_{\mathrm{MSE}} = \frac{1}{n}\sum_{i=1}^{n} \|\tilde{y}_i - y_i\|_2 \tag{4}$$

To overcome the platform effect, we utilized a discriminator $f_\varphi : \mathbf{z}_i \rightarrow (\mathbf{0},\mathbf{1})$ to distinguish if the graph is generated from pseudo-spots or SRT spots. Before the discriminator, there is an additional gradient reversal layer, making the gradient reverse during backpropagation. The final outcome is that the discriminator tries to minimize the domain discriminator loss while the former encoder tries to maximize the domain discriminator loss. In this way, the encoder can extract common features for scRNA-seq and SRT. This process is called adversarial domain adaptation. The true and predicted domain labels of node $i$ are represented as $m_i$ and $\tilde{m}_i$ ($\tilde{m}_i = 1$ and $m_i = 1$ if the nodes represent SRT spots), respectively. The cross-entropy loss of the domain discriminator is represented as:

$$L_{\mathrm{CE}} = -\frac{1}{n}\sum_{i=1}^{n}(m_i \log(\tilde{m}_i) + (1-m_i)log(1-\tilde{m}_i)) \tag{5}$$

Another task is to learn the whole cell-type fractions at the sample level. We calculated the predicted cell-type fraction by averaging the predicted cell-type proportions of all pseudo-spots in the graph. Similarly, we obtained the true cell-type fraction by approximately averaging the true cell-type proportions of all pseudo-spots (instead of summing by all single cells, see differences in the next section). HarmoDecon encourages minimizing the difference between predicted and true cell-type fractions:

$$L_{\mathrm{sample}} = \frac{1}{n^2}\|\sum_{i=1}^{n}\tilde{y}_i - \sum_{i=1}^{n} y_i\|_2 \tag{6}$$

We also used an entropy-based loss, which penalizes overbalanced cell-type proportions (e.g. $\frac{1}{N_K}$) and encourages generating dominant cell type(s) (e.g. $> 50\%$) for the individual pseudo-spot (first term) and across all pseudo-spots for each graph (second term).

$$\begin{aligned} L_{\mathrm{entropy}} = &-\frac{1}{n}\sum_{j=1}^{CT}\sum_{i=1}^{n} y_{i,CT}\log(y_{i,CT}) \\ &-\sum_{j=1}^{CT}\left(\frac{1}{n}\sum_{i=1}^{n} y_{i,CT}\right)\log\left(\frac{1}{n}\sum_{i=1}^{n} y_{i,CT}\right) \end{aligned} \tag{7}$$

The final loss function on pseudo-spots can be written as $L = L_{recon} + 1000 * L_{MSE} + L_{CE} + 1000 * L_{sample} + 10 * L_{entropy}$. For the graphs from SRT spots, the final loss function is $L = L_{recon} + L_{CE}$. In the inference procedure, we provide HarmoDecon with both spatial and gene expression graphs of pseudo-spots to generate $\tilde{y}_{spatial}$ and $\tilde{y}_{expression}$. The final cell-type proportion is calculated by

$$\tilde{y}_{pred} = \frac{\tilde{y}_{spatial} + \tilde{y}_{expression}}{2} \tag{8}$$

HarmoDecon is trained by Adam optimizer with a learning rate = 0.001 on 20 epochs. Within each epoch, three types of graphs are trained in order: First, train with 250 gene expression graphs, each with 200 pseudo-spots, then the gene expression graph and the spatial graph consisting of SRT spots.

Noted that we did not utilize a validation set or an early stopping strategy, since splitting the pseudo-spots generated from the same sampling strategy did not show improvement in the loss curve within 20 epochs (Fig. S28, available as supplementary data at *Bioinformatics* online). And Cell-type labels (if they have) in the tested SRT spots were completely unseen during training.

For a comprehensive understanding of data propagation within neural networks, graph construction, and evaluation metrics, please refer to the Notes, available as supplementary data at *Bioinformatics* online.

## 3 Results

### 3.1 The architecture of HarmoDecon and cell-type deconvolution workflow

HarmoDecon is a semi-supervised deep learning model that utilizes GMGCN architecture to perform accurate cell-type deconvolution in sequencing-based SRT data (Fig. 1). GMGCN (Dilokthanakul *et al.* 2016) leverages the graph structure to update node features by message passing and assumes the node embeddings follow a Gaussian mixture model. The rationale behind integrating GMGCN into HarmoDecon lies in its inherent ability to capture the spatial and gene expression similarities among SRT spots/pseudo-spots and reflect the fact that SRT spots are from different spatial domains.

The model is trained using pseudo-spots generated from scRNA-seq data with known cell-type fractions (Fig. 1a) and SRT spots with spatial locations (Fig. 1b). After building graphs from these spots (Section 2), HarmoDecon accepts three kinds of graphs as input (Fig. 1c). They are (i) one spatial graph for SRT spots, (ii) one gene expression graph for SRT spots, and (iii) 250 gene expression graphs for pseudo-spots. Within one training epoch, the HarmoDecon model first processes 250 gene expression graphs from pseudo-spots, then the spatial graph and expression graph from SRT spots.

The parameters of GMGCN are optimized through a set of specialized loss functions (Section 2): (i) Cross-entropy loss ($L_{CE}$): HarmoDecon includes a domain discriminator to differentiate if a given graph derives from scRNA-seq (pseudo-spots) or SRT (SRT spots). By reversing the gradient during backpropagation, the encoder of GMGCN can learn common features for these two platforms to fool the discriminator. This adversarial training design can mitigate the platform effect. (ii) Reconstruction loss ($L_{recon}$): HarmoDecon is encouraged to reconstruct the graph structure from node embeddings; (iii) sample loss ($L_{sample}$): HarmoDecon strives to minimize the difference between the predicted and expected sample-level cell-type fractions, which are calculated by averaging the cell-type proportions of all pseudo-spots. (iv) Entropy loss ($L_{entropy}$): HarmoDecon encourages the prediction of predominant cell types (low information entropy) for SRT spots. (v) HarmoDecon seeks to minimize the mean squared error (MSE) between the predicted and expected cell-type proportions for pseudo-spots. The MSE loss ($L_{MSE}$) is directly tied to the cell-type deconvolution task and serves as the primary loss function. Noted that HarmoDecon avoids supervising the proportions of SRT

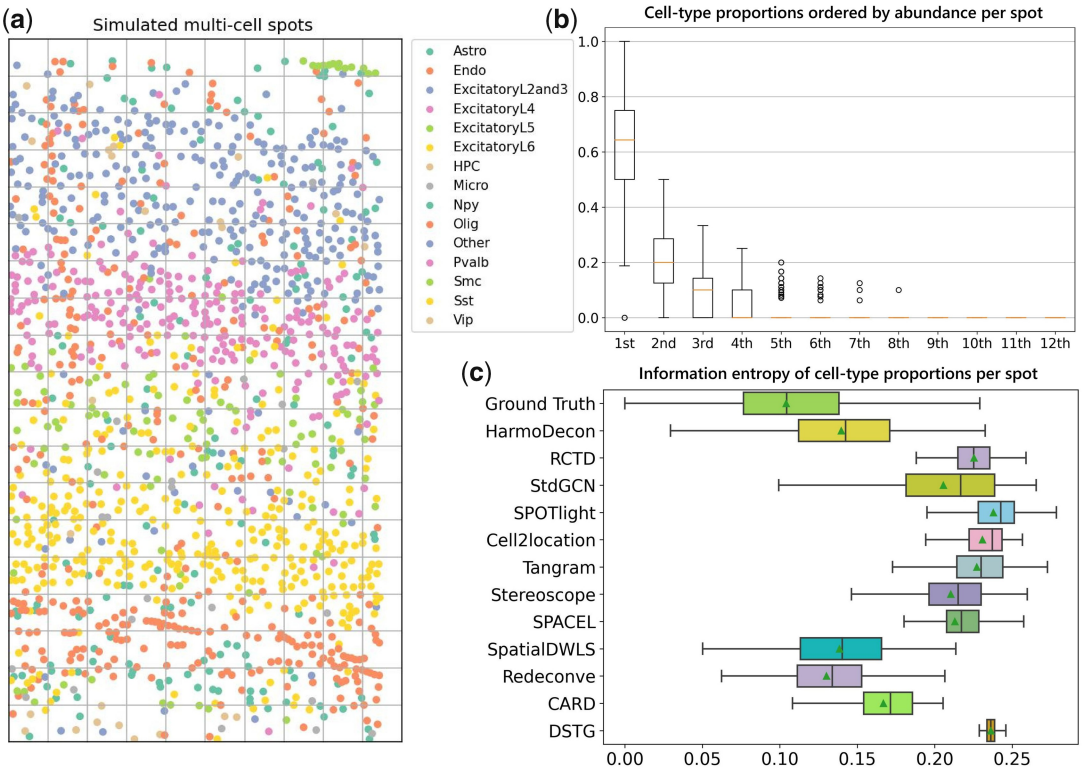


**Figure 2.** Preliminary studies on the simulated multi-cell spots from the STARmap dataset. (a) Simulate multi-cell spots on the STARmap dataset. We simulated multi-cell spots by dividing the landscape into quadrilateral grids, each representing a rectangular grid containing 1–16 cells. The gene expression profile for each simulated spot was calculated by aggregating the gene expression of all involved cells. Dots with different colors represent single cells from different cell types. (b) Boxplots of cell-type proportions ordered by abundance per spot ($n = 189$) in the simulated STARmap data. We sort the number of abundance of each cell type by spot. The $i$th box of the plot represents the cell type with the $i$th abundance instead of a specific cell type. Three cell types (Other, Npy and HPC) not occurring in the reference scRNA-seq are excluded. (c) The box plot of information entropy of cell-type proportions predicted by different tools ($n = 189$). Three cell types (Other, Npy and HPC) are excluded. A lower entropy value indicates a distribution with fewer dominant cell types, while a higher value suggests more balanced cell-type proportions.

spots directly. Only $L_{CE}$ and $L_{recon}$ are calculated for graphs from both SRT spots and pseudo-spots, while $L_{sample}$, $L_{entropy}$ and $L_{MSE}$ are only for graphs from pseudo-spots (Fig. 1c).

In the inference procedure (Fig. 1d), HarmoDecon averages cell-type proportions predicted from the spatial and gene expression graphs. Finally, HarmoDecon offers functions for drawing heat maps for individual cell types and pie charts of the cell-type proportion within each SRT spot.

## 3.2 HarmoDecon achieves better cell-type deconvolution on simulated multi-cell spots from STARmap and osmFISH

To simulate SRT spots with known cell-type proportions, we generated synthetic multi-cell spots by aggregating single cells from STARmap (Wang *et al.* 2018b) and osmFISH (Codeluppi *et al.* 2018) technologies (Section 2, Fig. 2). HarmoDecon was benchmarked against 11 existing deconvolution tools—RCTD, STdGCN, SPOTlight, Cell2Location, Tangram, Stereoscope, SPACEL, SpatialDWLS, Redeconve, CARD, and DSTG—using five evaluation metrics: the Pearson correlation coefficient (PCC), structural similarity index measure (SSIM), Jensen-Shannon divergence (JSD), root-mean-square error (RMSE), and a comprehensive rank-based accuracy score (AS). The AS provides a holistic evaluation by considering the ranking of each tool across PCC, SSIM, JSD, and RMSE metrics (Li *et al.* 2022) (Section 2). The scRNA-seq datasets used by these deconvolution tools were downloaded from the same tissue as those used to generate STARmap (Tasic *et al.* 2018) (from the mouse visual cortex) and osmFISH (Yao *et al.* 2021) (from the mouse somatosensory cortex) datasets. For STARmap, we only kept 12 common cell types that both scRNA-seq and SRT have during evaluation. Three cell types (Other, Npy and HPC) are excluded.

In the simulated multi-cell spots from both STARmap and osmFISH technologies, HarmoDecon outperformed all other state-of-the-art tools across all five evaluation metrics (Fig. 3b and d). HarmoDecon achieved the highest AS values (STARmap: 0.76, osmFISH: 0.77), significantly surpassing the second-best tools: RCTD for STARmap ($P$-value = 7.85E−3, Fig. S5, available as supplementary data at *Bioinformatics* online) and Redeconve for osmFISH ($P$-value = 4.88E−6, Fig. S6, available as supplementary data at *Bioinformatics* online). Spatial scatter pie charts showed that the cell-type proportions estimated by HarmoDecon most closely matched the ground truth in the STARmap (Fig. 3a) and osmFISH (Fig. 3c) simulated datasets. In contrast, other methods produced an over-balanced mixture of cell types per spot, which was quite different from the ground truth. The result of HarmoDecon on the STARmap data demonstrated that areas with a high prevalence of eL2/3, eL4, eL5, and eL6 cell types corresponded well with the expected excitatory spatial regions (Fig. 3e). In contrast, other methods failed to show clear distributions of these cell types in the spatial domains (Fig. S7, available as supplementary data at *Bioinformatics* online). A similar trend was observed with the osmFISH dataset, where

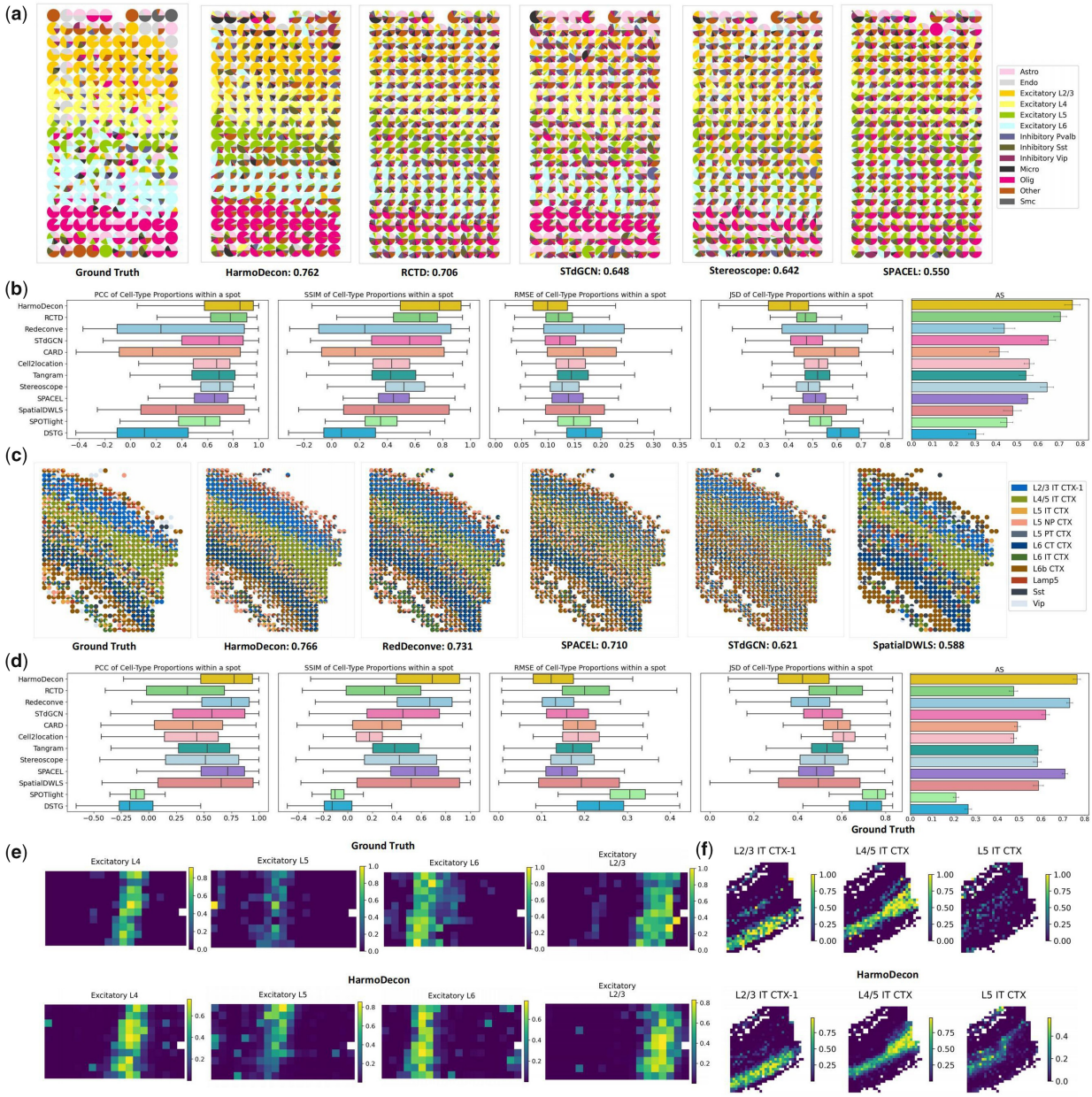


**Figure 3.** Cell-type deconvolution results on simulated multi-cell spots from STARmap and osmFISH. Spatial scatter pie plots show the cell type proportions for each spot as predicted by different methods on the simulated STARmap (a) and osmFISH (c) datasets. The corresponding AS is shown below each plot. Boxplots [$n = 189$ (STARmap), 737 (osmFISH)] of the four evaluation metrics (PCC, SSIM, RMSE, JSD) and bar plots of AS for 12 benchmarking methods on the STARmap (b) and osmFISH (d) datasets. The bar plots include error bars representing a 95% confidence interval. The proportions of corresponding excitatory neurons predicted by HarmoDecon in the simulated spots from STARmap (e) and osmFISH (f).

HarmoDecon accurately identified regions predominantly composed of L2/3 IT CTX1, L4/5 IT CTX, and L6 CT CTX cell types within their respective L2/3, L4/5, and L6 domains. Other methods struggled to correctly align these cell types with their specific domains (Fig. S8, available as supplementary data at *Bioinformatics* online).

To further assess cross-tissue robustness, we extended benchmarking to the MOSTA mouse embryo dataset (Chen *et al.* 2022a) (Figs S24 and S25, available as supplementary data at *Bioinformatics* online), which spans diverse tissues and organs. HarmoDecon achieves the highest scores across all five metrics (PCC, SSIM, RMSE, JSD, and AS), demonstrating consistent generalizability in complex multi-organ spatial contexts.

## 3.3 HarmoDecon captures accurate sample-level cell-type fractions

We calculated the sample-level cell-type fractions for single-cell SRT data from STARmap and osmFISH (Section 2, Ground Truth shown in Fig. 4a and c). We observed the sample-level common and rare cell types distributed across different anatomical layers (Fig. 4a and c, left). The sample-level common cell-types dominated the spots in the relevant anatomical layers (STARmap: Excitatory L2/3, Excitatory L4, Excitatory L5, Excitatory L6; osmFISH: L2/3 IT CTX-1, L4/5 IT CTX, L6 CT CTX), while peripheral regions were enriched with rare cell types.

We then performed a linear regression analysis to evaluate the concordance between predicted and ground truth sample-

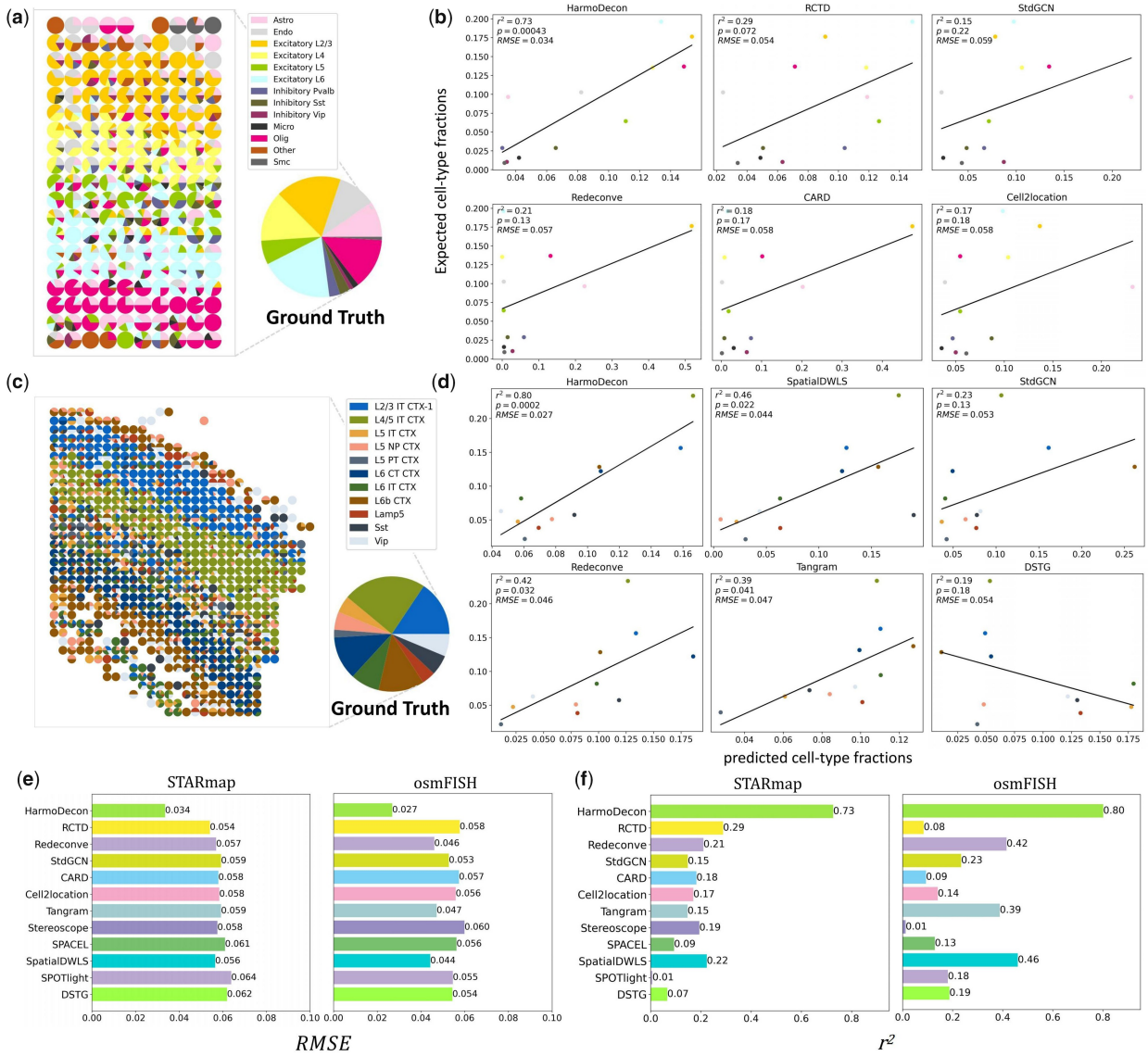


**Figure 4.** Benchmarking cell-type deconvolution tools for estimating sample-level cell-type fractions. Spatial scatter pie charts illustrate cell-type proportions and the sample-level cell-type fractions (Ground Truth) in simulated datasets from STARmap (a) and osmFISH (c). Linear regression plots compare the performance of six deconvolution tools with the highest $r^2$ values in predicting sample-level cell-type fractions for STARmap (b) and osmFISH (d). The y-axis shows the expected (Ground Truth) fractions, and the *x*-axis represents the predicted fractions obtained by averaging proportions across spots. Bar charts compare the performance of different deconvolution tools with respect to RMSE (e) and $r^2$ (f).

level cell-type fractions of different tools. HarmoDecon demonstrated the highest accuracy, achieving the best $r^2$ and RMSE values for both STARmap ($r^2$ =0.73, RMSE = 0.034, *P*-value = 4E−4; Fig. 4b) and osmFISH ($r^2$ =0.80, RMSE = 0.027, *P*-value = 0.0269; Fig. 4d) datasets (Fig. S3, available as supplementary data at *Bioinformatics* online). These results substantially outperformed the second-best tools (STARmap: RCTD, $r^2$=0.29, RMSE = 0.054; osmFISH: SpatialDWLS, $r^2$=0.46, RMSE = 0.043). Some large discrepancies between predicted and true cell-type fractions were noted from the results of the other tools. In the STARmap dataset, the most common cell types were Excitatory L2/3, L6, Olig, and L4. Tools like STdGCN and Cell2location notably underestimated the abundances of Excitatory L2/3 and L6, while Redeconve and CARD underestimated Olig and L4. Conversely, RCTD overestimated certain rare cell types, such as Excitatory L5 and Inhibitory Pvalb. A similar pattern emerged with the osmFISH dataset, where STdGCN and Redeconve underestimated the most prevalent cell type, L4/5 IT CTX, while DSTG inverted the overall trend by predicting higher proportions for rare cell types and lower for common ones, resulting in a negative correlation with the true fractions.

To assess HarmoDecon's ability to derive biologically meaningful insights at the sample level, we analyzed cell-type fractions across developmental stages using the 10x Visium human fetal limb dataset (Zhang *et al.* 2024). Our analysis revealed coherent temporal patterns in cellular composition that recapitulate established principles of limb development (Fig. S27, available as supplementary data at *Bioinformatics* online). The predicted sample-level cell-type fractions showed a progressive decline in undifferentiated mesenchymal cell populations accompanied by increasing proportions of terminally differentiated cell types, including Schwann cells and muscle cells. This transition mirrors the expected differentiation trajectory during normal limb morphogenesis. Intermediate progenitor populations exhibited dynamic

fluctuations across developmental timepoints, consistent with their transient role in tissue patterning. Spatial analysis revealed organization patterns that correspond to known morphogenetic fields, with proximal-to-distal and dorsal-to-ventral gradients matching established developmental axes.

### 3.4 HarmoDecon generates predominant cell types for each spot

We used information entropy to evaluate if the predicted cell-type proportions from deconvolution tools were overbalanced (Fig. 2c). A lower entropy value indicates a distribution with fewer dominant cell types, while a higher value suggests more balanced cell-type proportions. Among the methods evaluated, HarmoDecon, SpatialDWLS, and Redeconve yielded entropy values that most closely matched those of the ground truth. Although SpatialDWLS and Redeconve produced lower information entropy, their overall performance was worse than that of HarmoDecon (Fig. 3b and Fig. S5, available as supplementary data at *Bioinformatics* online). HarmoDecon effectively inferred dominant cell types for each SRT spot, consistent with our observations in single-cell resolution SRT datasets (Fig. S2, available as supplementary data at *Bioinformatics* online).

### 3.5 HarmoDecon enables accurate spatial domain clustering on legacy SRT datasets

We further evaluated the performance of spatial domain clustering on the cell-type deconvolution results using two SRT datasets from legacy SRT technique: Mouse Olfactory Bulb (MOB) (Ståhl *et al.* 2016) and Human Melanoma (Thrane *et al.* 2018) datasets. The matched scRNA-seq data were downloaded from two other studies (Tirosh *et al.* 2016, Tepe *et al.* 2018). Spatial domain labels for the spots were assigned by applying K-means clustering to the predicted cell-type proportions, with the value of K determined based on the ground truth.

The Mouse Olfactory Bulb (MOB) dataset consists of four anatomical layers: the granule cell layer (GCL), mitral cell layer (MCL), glomerular layer (GL), and olfactory nerve layer (ONL). Compared to other methods (Fig. 5a, Fig. S9, available as supplementary data at *Bioinformatics* online), HarmoDecon accurately reconstructed the original spatial domain structure, achieving a strong alignment with the ground truth (ARI: 0.63, purity: 0.84, Fig. 5c). Competing tools like STdGCN, Redeconve, and RCTD failed to distinguish between the three outer layers (MCL, GL, ONL). While SPACEL, SpatialDWLS, and CARD demonstrated improved clustering performance, they were unable to clearly delineate the boundaries between layers, and their deconvolution results within the same domain showed lower accuracy.

We found that only HarmoDecon was able to accurately capture the dominant cell types within their corresponding spatial domains. For example, olfactory sensory neurons (OSNs), which are expected to be enriched in the ONL, were predicted by HarmoDecon to make up over 70% of the cell-type proportions across all SRT spots in the ONL (Fig. 5a, Fig. S26, available as supplementary data at *Bioinformatics* online). Moreover, HarmoDecon was the only method that delineated a distinct boundary for the GL (Fig. 5a, in bright green), with an enrichment of periglomerular cells (PGCs) and mitral/tufted cells (M/TCs). In comparison, the second-best tool, SPACEL, struggled to reconstruct a continuous GL, while the remaining tools frequently misclassified spots as part of the GL.

Based on the H&E image, the Human Melanoma dataset demonstrated four spatial domains (Fig. 5d, spatial clusters): stroma (cluster 1, red), core melanoma (cluster 2, blue), the border area between the lymphoid and tumor tissues (cluster 3, purple) and lymphoid tissue (cluster 4, orange). HarmoDecon, RCTD, and SPACEL outperformed the other tools and could identify the boundary between core melanoma and the border area. RCTD misclassified spots in benign regions, which were primarily composed of cancer cells, leading to an erroneous expansion of the melanoma regions (Fig. 5e, Fig. S10, available as supplementary data at *Bioinformatics* online, in teal color). SPACEL curated smaller lymphoid regions, with several spots belonging to the lymphoid tissue (Fig. 5d, manual annotation) assigned to the stroma.

### 3.6 HarmoDecon captures correlations inside cancer regions on 10X Visium SRT datasets

To evaluate the performance of HarmoDecon across different platforms and tissue types, we apply it to two human breast cancer samples sequenced using the 10X Visium technology (10x Genomics 2020) (BRCA_1: Fig. 6c and BRCA_2: Fig. 6f). We downloaded scRNA-seq data for matching breast cancer subtypes (BRCA_1: ER+HER2+; BRCA_2: HER2+) and annotated cell types using human breast cancer atlas (Wu *et al.* 2021).

For the BRCA_1 sample, we examined the colocalization of cancer cells with known cancer marker genes. Ten well-documented breast cancer marker genes were selected [PIP (Urbaniak *et al.* 2018), SHISA2 (Cheishvili *et al.* 2015), PDZK1IP1 (Garcia-Heredia *et al.* 2017), PLEKHS1 (Weinhold *et al.* 2014), NAT1 (Johansson *et al.* 2012), TFAP2C (Woodfield *et al.* 2007), NPNT (Wang *et al.* 2018a), SCUBE2 (Chen *et al.* 2018), ASCL2 (Xu *et al.* 2017), DNAJC1 (Zoppino *et al.* 2018)], whose expression is expected to correlate strongly with the presence of cancer epithelial cells. We observed all ten marker genes showed high expression levels in the lower part of the tissue section, with significantly lower expression in the upper part (Fig. 6a and Fig. S11, available as supplementary data at *Bioinformatics* online), suggesting that cancer epithelial cells are also concentrated at the bottom. Only HarmoDecon (Fig. 6a, Fig. S12, available as supplementary data at *Bioinformatics* online) successfully aligned the gene expression patterns of these marker genes with the distribution of cancer epithelial cells, while other methods failed to do so. We also calculated PCC between the gene expression profiles of marker genes and the predicted cancer epithelial cell proportions. HarmoDecon demonstrated the highest PCC, which was significantly better than the second-best tool (SPACEL, $P$-value = 0.002, Fig. 6b). CARD, RCTD, SPACEL and SpatialDWLS tended to assign high proportions of cancer epithelial cells to all spots. Redeconve failed to map the spatial distribution of normal and cancer cells, showing the opposite trend. STdGCN failed to capture any spatial distribution preferences for cancer epithelial cells.

We then investigated if the distribution of cancer epithelial cells matched with the carcinoma regions in the BRCA_2 dataset. Cancer and normal regions were annotated based on the H&E image (Section 2, Fig. 6d). HarmoDecon, SpatialDWLS, and Redeconve all enriched spots dominated by cancer epithelial cells in the cancerous regions (Fig. S13,

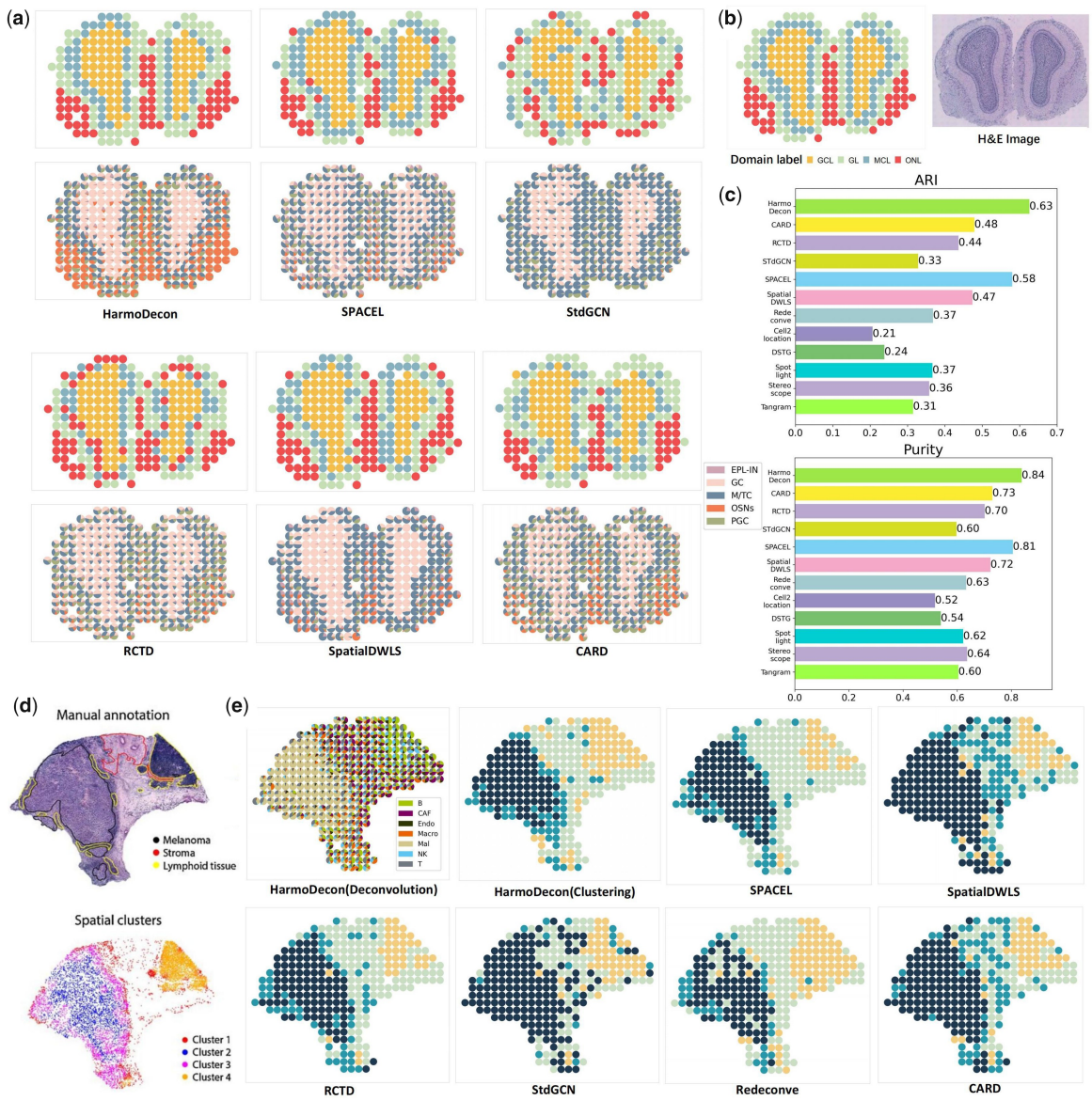


**Figure 5.** The performance of deconvolution tools on spatial domain clustering. (a) Spatial domain clustering dot plots and the scatter pie charts of spot cell-type proportions on the MOB dataset. (b). The ground truth of spatial domain (Long *et al.* 2023) and H&E pathological image (Ståhl *et al.* 2016) of the MOB dataset. (c) The values of ARI and Purity of spatial domain clustering on the MOB dataset. (d) The H&E pathological image and spatial domain annotation of the Human Melanoma dataset [credit by Thrane *et al.* (2018)]. (e) Spatial domain clustering dot plots show the spatial domains inferred from the results of different deconvolution tools on the Human Melanoma dataset. The scatter pie chart (upper left) shows the cell-type proportions inferred by HarmoDecon.

available as supplementary data at *Bioinformatics* online). HarmoDecon produced a clear boundary between cancerous and normal regions, with far fewer spots from normal regions predicted to contain cancer epithelial cells (Fig. 6d, Fig. S14, available as supplementary data at *Bioinformatics* online). It also generated the highest median proportion of cancer epithelial cells (0.786) in cancerous regions and the second-lowest median value (0.003) in normal regions. Although Tangram had the smallest median value (0.0002) in normal regions, its median proportion in cancerous regions (0.272) was significantly lower than that of HarmoDecon (Fig. 6g).

## 4 Discussion

Spatial transcriptomics offers valuable insights into spatial biology, allowing us to understand gene expression profiles in tissue spatial landscapes. Some SRT technologies cannot achieve single-cell resolution, and many methods have been developed for cell-type deconvolution. However, despite the advancements of existing tools, our preliminary studies revealed three biases: 1. overbalanced cell-type proportions predicted in individual spots; 2. sample-level cell-type fractions from SRT data fail to align with the expected cell-type fractions; 3. platform effects between scRNA-seq and SRT data; In this study, we introduced HarmoDecon, a novel semi-supervised deep learning model designed for cell-type deconvolution in SRT data. HarmoDecon addresses these three biases by generating pseudo-spots from scRNA-seq data and utilizing GMGCN with specific loss functions. We performed extensive experiments on different SRT technologies and observed that HarmoDecon outperformed 11 state-of-the-art cell-type deconvolution tools. We also estimate and

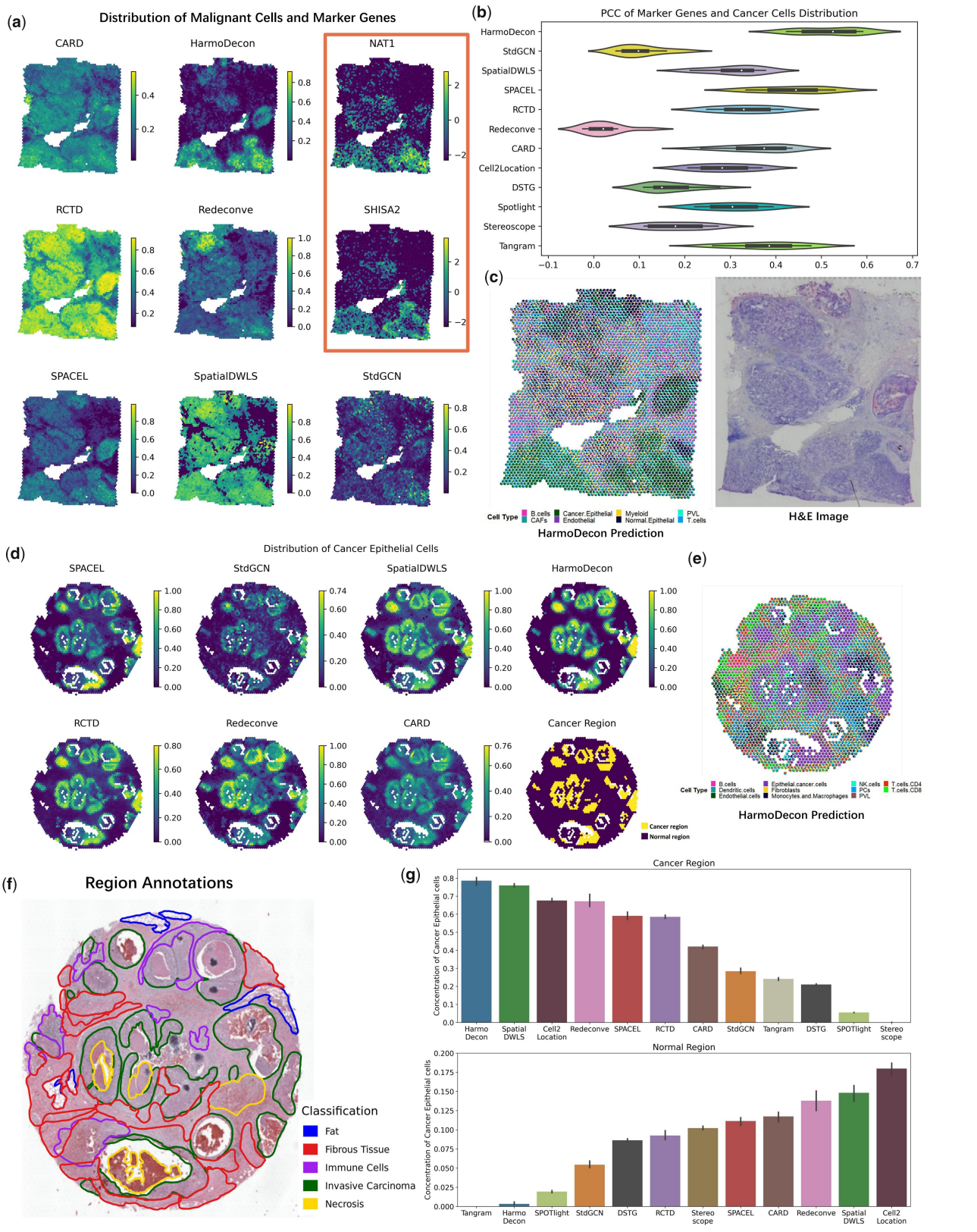


**Figure 6.** The performance of HarmoDecon on two breast cancer 10X Visium datasets. (a) Distributions of cancer epithelial cells and gene expression of NAT1 and SHISA2 on the BRCA_1 dataset. (b) The Violin plot of PCC between the gene expression profiles of 10 marker genes and cancer epithelial cell distribution on the BRCA_1 dataset. (c) The pie chart plots of cell-type proportions predicated by HarmoDecon and the H&E pathological image of the BRCA_1 dataset. (d) Ground truth of cancer and normal regions and distributions of cancer epithelial cells from different deconvolution methods on the BRCA_2 dataset. (e) The pie chart of cell-type proportions predicated by HarmoDecon on the BRCA_2 dataset. (f) Region annotation of the BRCA_2 dataset. (g) Bar charts of the proportion of cancer epithelial cells in the cancer region (upper) and normal region (lower) inferred by different deconvolution methods in the BRCA_2 dataset.

compare the runtime and memory consumption of deconvolution tools (Table S2, available as supplementary data at *Bioinformatics* online, Fig. S30, available as supplementary data at *Bioinformatics* online). HarmoDecon is positioned in the moderate range in terms of time and memory efficiency when compared to the other evaluated methods.

Compared to existing graph neural network-based deconvolution tools like DSTG and STdGCN, HarmoDecon offers several methodological novelties. First, HarmoDecon constructs multiple smaller graphs instead of a single large graph (as in STdGCN), improving memory efficiency and acting as a form of data augmentation. While STdGCN and DSTG suggest 30 000 and 1500 pseudo-spots for optimal performance, respectively, HarmoDecon achieves robust results with 50 000 pseudo-spots (Fig. S16c, available as supplementary data at *Bioinformatics* online), albeit with potential trade-offs in processing time. Moreover, HarmoDecon uniquely integrates multiple loss functions (Entropy Loss, Sample Loss, and Cross-Entropy Loss of the Domain Discriminator) to address overbalancing, sample-level fraction alignment, and platform effects.

We performed comprehensive ablation studies to evaluate the significance of the loss functions used in HarmoDecon (Fig. S15, available as supplementary data at *Bioinformatics* online). Among all the loss functions, the entropy loss proved to be the most important factor in improving the performance of HarmoDecon (Fig. S15, available as supplementary data at *Bioinformatics* online, w/o_entropy; Fig. S23, available as supplementary data at *Bioinformatics* online). In contrast, sample loss (Fig. S15, available as supplementary data at *Bioinformatics* online, w/o_sample) and domain adaptation loss (Fig. S15, available as supplementary data at *Bioinformatics* online, w/o_domain) had minor effects in reducing error for cell-type proportions for each SRT spot. We discuss how different choices of weights of the entropy loss and sample loss might impact the model's performance (Fig. S23, available as supplementary data at *Bioinformatics* online). Though the sample loss has minor improvements in the metrics, it primarily affects the accuracy of sample-level cell-type fractions rather than spot-level proportions. For example, HarmoDecon without the sample loss led to the underestimation of certain cell types (e.g. L6 IT CTX and L6b CTX) in the osmFISH dataset, causing predicted cell-type fractions to deviate from the ground truth (Fig. S18, available as supplementary data at *Bioinformatics* online). To assess the domain adaptation loss, we performed principal component analysis (PCA) on SRT spots and pseudo-spot latent embeddings from the STARmap and MOB datasets. The results show that domain adaptation loss effectively mitigates batch effects between SRT and scRNA-seq technologies (Fig. S19, available as supplementary data at *Bioinformatics* online). Quantitative validation shows HarmoDecon's superior ability to mitigate platform effects, evidenced by the lowest Silhouette Score between SRT and pseudo-spot embeddings compared to DSTG and STdGCN. And the platform effects are indeed alleviated by deploying the domain loss.

Additionally, we investigated the influence of hyperparameters on both sampling and training procedures. When building the spatial graph using K-nearest neighbors, we observed that increasing K led to more connections but also introduced errors (Fig. S17a, available as supplementary data at *Bioinformatics* online). This may be due to oversmoothing, a well-known issue in graph models (Rusch *et al.* 2023). The model was sensitive to the mean number of cells and the mean number of cell types per pseudo-spot (Fig. S16a and b, available as supplementary data at *Bioinformatics* online). In the ablation study, we observed that HarmoDecon performed best when the mean number of cells and number of cell types across pseudo-spots was close to those across SRT spots.

HarmoDecon uses spatial and gene expression graphs to capture spatial proximity and gene expression similarities between spots. Our results reveal that averaging the cell-type proportions inferred from both graphs leads to significant improvements across all datasets and evaluation metrics tested (Fig. S20, available as supplementary data at *Bioinformatics* online). This strategy is based on the fact that spatially adjacent spots and spots with high gene expression similarities are likely to share similar cell-type proportions. Similar findings have been reported in recent studies, including (Ma and Zhou 2022, Vahid *et al.* 2023, Li and Luo 2024).

To date, only a few deconvolution tools can handle multi-slice SRT data simultaneously. While SPACEL provides a pipeline for 3D SRT data analysis, its integrated deconvolution tool, Spoint, is limited to single-slice data. Currently, HarmoDecon also operates on single-slice SRT data, but we plan to extend its functionality to support multi-slice datasets in the future. We will build spatial and gene expression graphs by considering spatially adjacent spots as well as spots with high gene expression similarities across different slices.

## Acknowledgements

We thank the Research Grant Council (RGC) Hong Kong and Research Committee of Hong Kong for their kind support of this project.

## Author contributions

Zirui Wang (Conceptualization [lead], Data curation [lead], Formal analysis [lead], Funding acquisition [lead], Investigation [lead], Methodology [lead], Project administration [equal], Software [lead], Validation [lead], Visualization [lead], Writing—original draft [lead], Writing—review & editing [equal]), Ke Xu (Conceptualization [equal], Data curation [supporting], Investigation [equal], Methodology [equal]), Yang Liu (Conceptualization [equal], Methodology [supporting], Software [supporting], Writing—review & editing [supporting]), Yu Xu (Conceptualization [supporting], Visualization [supporting], Writing—review & editing [supporting]), and Lu Zhang (Conceptualization [equal], Investigation [equal], Methodology [equal], Project administration [lead], Resources [lead], Supervision [lead], Writing—original draft [equal], Writing—review & editing [lead])

## Supplementary data

Supplementary data is available at *Bioinformatics* online.

Conflict of interest: None declared.

## Funding

The design of the study, the collection, analysis, and interpretation of the data were partially supported by the Young Collaborative Research grant [C2004-23Y], HMRF

[11221026], and HKBU Start-up Grant Tier 2 [RC-SGT2/19-20/SCI/007].

## Data availability

The datasets used in this study are all publicly available:

1) Mouse visual cortex (STARmap): https://www.starmapresources.com/data, with matched scRNA-seq from https://portal.brain-map.org/atlases-and-data/rnaseq/mouse-v1-and-alm-smart-seq.
2) Mouse somatosensory cortex (osmFISH): http://linnarssonlab.org/osmFISH, with cell-type labels annotated by Chen *et al.* (2022b), matched scRNA-seq from https://portal.brain-map.org/atlases-and-data/rnaseq/mouse-whole-cortex -and-hippocampus-smart-seqSSp Region.
3) Mouse olfactory bulb (Legacy ST): http://www.spatialtranscriptomicsresearch.org, with matched scRNA-seq from GSE121891 in the GEO database.
4) Human melanoma (Legacy ST): https://www.spatialresearch.org/resources-published-datasets/doi-10-1158-0008-5472-can-18-0747/, with matched scRNA-seq from GSE72056 in the GEO database.
5) Human breast cancer ER+/HER2+ (10X Visium): https://support.10xgenomics.com/spatial-gene-expression/datasets/1.1.0/V1_Breast_Cancer_Block_A_Section_1, with matched scRNA-seq from GSE176078: CID3586, CID4066 in the GEO database.
6) Human breast cancer HER2+ (10X Visium): https://cf.10xgenomics.com/samples/spatial-exp/1.3.0/Visium_FFPE_Human_Breast_Cancer/Visium_FFPE_Human_Breast_Cancer_web _summary.html, with matched scRNA-seq from GSE176078: CID3921, CID45171, CID3838 in the GEO database.

## Code availability

The HarmoDecon scripts are available at https://github.com/ericcombiolab/HarmoDecon/tree/main.

The custom code for reproducing results in the experiments is available at https://github.com/ericcombiolab/HarmoDecon/tree/main/scripts. We have published our code on the Figshare, which provides an archival DOI https://doi.org/10.6084/m9.figshare.28006364.v2.

## References

10. x Genomics. *Visium Spatial Gene Expression*. Pleasanton, California, USA: 10x Genomics, Inc., 2020.

Andersson A, Bergenstråhle J, Asp M *et al.* Single-cell and spatial transcriptomics enables probabilistic inference of cell type topography. *Commun Biol* 2020;**3**:565.

Arora R, Cao C, Kumar M *et al.* Spatial transcriptomics reveals distinct and conserved tumor core and edge architectures that predict survival and targeted therapy response. *Nat Commun* 2023;**14**:5029.

Biancalani T, Scalia G, Buffoni L *et al.* Deep learning and alignment of spatially resolved single-cell transcriptomes with Tangram. *Nat Methods* 2021;**18**:1352–62. https://doi.org/10.1038/s41592-021-01264-7

Cable DM, Murray E, Zou LS *et al.* Robust decomposition of cell type mixtures in spatial transcriptomics. *Nat Biotechnol* 2022;**40**:517–26.

Cheishvili D, Stefanska B, Yi C *et al.* A common promoter hypomethylation signature in invasive breast, liver and prostate cancer cell lines reveals novel targets involved in cancer invasiveness. *Oncotarget* 2015;**6**:33253–68.

Chen A, Liao S, Cheng M *et al.* Spatiotemporal transcriptomic atlas of mouse organogenesis using DNA nanoball-patterned arrays. *Cell* 2022a;**185**:1777–92.e21.

Chen J, Liu, W, Luo T *et al.* A Comprehensive Comparison on Cell-Type Composition Inference for Spatial Transcriptomics data. *Brief Bioinform* 2022b;**23**:1477–54. https://doi.org/10.1093/bib/bbac245

Chen J-H, Kuo K-T, Bamodu OA *et al.* Upregulated SCUBE2 expression in breast cancer stem cells enhances triple negative breast cancer aggression through modulation of notch signaling and epithelial-to-mesenchymal transition. *Exp Cell Res* 2018;**370**:444–53.

Close JL, Long BR, Zeng H. Spatially resolved transcriptomics in neuroscience. *Nat Methods* 2021;**18**:23–5.

Codeluppi S, Borm LE, Zeisel A *et al.* Spatial organization of the somatosensory cortex revealed by osmFISH. *Nat Methods* 2018;**15**:932–5.

Dilokthanakul N, Mediano P, Garnelo M *et al.* Deep unsupervised clustering with gaussian mixture variational autoencoders. arXiv, arXiv:1611.02648, 2016, preprint: not peer reviewed.

Dong K, Zhang S. Deciphering spatial domains from spatially resolved transcriptomics with an adaptive graph attention auto-encoder. *Nat Commun* 2022;**13**:1739.

Dong R, Yuan G-C. SpatialDWLS: accurate deconvolution of spatial transcriptomic data. *Genome Biol* 2021;**22**:145.

Elosua-Bayes M, Nieto P, Mereu E *et al.* SPOTlight: seeded NMF regression to deconvolute spatial transcriptomics spots with single-cell transcriptomes. *Nucleic Acids Res* 2021;**49**:e50.

Eng C-HL, Lawson M, Zhu Q *et al.* Transcriptome-scale super-resolved imaging in tissues by RNA seqFISH+. *Nature* 2019;**568**:235–9.

Engblom C, Thrane K, Lin Q *et al.* Spatial transcriptomics of B cell and T cell receptors reveals lymphocyte clonal dynamics. *Science* 2023;**382**:eadf8486.

Ganin Y, Ustinova E, Ajakan H *et al. Domain-Adversarial Training of Neural Networks*. arXiv, 2016.

Garcia-Heredia JM, Lucena-Cacace A, Verdugo-Sivianes EM *et al.* The cargo protein MAP17 (PDZK1IP1) regulates the cancer stem cell Pool activating the notch pathway by abducting NUMB. *Clin Cancer Res* 2017;**23**:3871–83.

Hunter MV, Moncada R, Weiss JM *et al.* Spatially resolved transcriptomics reveals the architecture of the tumor-microenvironment interface. *Nat Commun* 2021;**12**:6278.

Johansson I, Nilsson C, Berglund P *et al.* Gene expression profiling of primary male breast cancers reveals two unique subgroups and identifies N-acetyltransferase-1 (NAT1) as a novel prognostic biomarker. *Breast Cancer Res* 2012;**14**:R31–15.

Kleshchevnikov V, Shmatko A, Dann E *et al.* Cell2location maps fine-grained cell types in spatial transcriptomics. *Nat Biotechnol* 2022;**40**:661–71.

Li B, Zhang W, Guo C *et al.* Benchmarking spatial and single-cell transcriptomics integration methods for transcript distribution prediction and cell type deconvolution. *Nat Methods* 2022;**19**:662. https://doi.org/10.1038/s41592-022-01480-9

Li H, Ma T, Hao M *et al.* Decoding functional cell–cell communication events by multi-view graph learning on spatial transcriptomics. *Brief Bioinform* 2023;**24**:bbad359.

Li Y, Luo Y. STdGCN: spatial transcriptomic cell-type deconvolution using graph convolutional networks. *Genome Biol* 2024;**25**:206.

Lohoff T, Ghazanfar S, Missarova A *et al.* Integration of spatial and single-cell transcriptomic data elucidates mouse organogenesis. *Nat Biotechnol* 2022;**40**:74–85.

Long Y, Ang KS, Li M *et al.* Spatially informed clustering, integration, and deconvolution of spatial transcriptomics with GraphST. *Nat Commun* 2023;**14**:1155.

Ma Y, Zhou X. Spatially informed cell-type deconvolution for spatial transcriptomics. *Nat Biotechnol* 2022;**40**:1349–59.
Moffitt JR, Bambah-Mukku D, Eichhorn SW *et al.* Molecular, spatial, and functional single-cell profiling of the hypothalamic preoptic region. *Science* 2018;**362**:eaau5324.
Rusch TK, Bronstein MM, Mishra S. A survey on oversmoothing in graph neural networks. arXiv, arXiv:2303.10993, 2023, preprint: not peer reviewed.
Sampath Kumar A, Tian L, Bolondi A *et al.* Spatiotemporal transcriptomic maps of whole mouse embryos at the onset of organogenesis. *Nat Genet* 2023;**55**:1176–85.
Shao X, Li C, Yang H *et al.* Knowledge-graph-based cell-cell communication inference for spatially resolved transcriptomic data with SpaTalk. *Nat Commun* 2022;**13**:4429.
Song Q, Su J. DSTG: deconvoluting spatial transcriptomics data through graph-based artificial intelligence. *Brief Bioinform* 2021; **22**:bbaa414.
Ståhl PL, Salmén F, Vickovic S *et al.* Visualization and analysis of gene expression in tissue sections by spatial transcriptomics. *Science* 2016;**353**:78–82.
Stickels RR, Murray E, Kumar P *et al.* Highly sensitive spatial transcriptomics at near-cellular resolution with Slide-seqV2. *Nat Biotechnol* 2021;**39**:313–9.
Tasic B, Yao Z, Graybuck LT *et al.* Shared and distinct transcriptomic cell types across neocortical areas. *Nature* 2018;**563**:72–8. https://doi.org/10.1038/s41586-018-0654-5
Tepe B, Hill MC, Pekarek BT *et al.* Single-Cell RNA-Seq of mouse olfactory bulb reveals cellular heterogeneity and Activity-Dependent molecular census of Adult-Born neurons. *Cell Rep* 2018; **25**:2689–703.e3. https://doi.org/10.1016/j.celrep.2018.11.034.
Thrane K, Eriksson H, Maaskola J *et al.* Spatially resolved transcriptomics enables dissection of genetic heterogeneity in stage III cutaneous malignant melanoma. *Cancer Res* 2018;**78**:5970–9. https://doi.org/10.1158/0008-5472.CAN-18-0747.
Tirosh I, Izar B, Prakadan SM *et al.* Dissecting the multicellular ecosystem of metastatic melanoma by single-cell RNA-seq. *Science* 2016; **352**:189–96. https://doi.org/10.1126/scienceaad0501.
Urbaniak A, Jablonska K, Podhorska-Okolow M *et al.* Prolactin-induced protein (PIP)-characterization and role in breast cancer progression. *Am J Cancer Res* 2018;**8**:2150–64.
Vahid MR, Brown EL, Steen CB *et al.* High-resolution alignment of single-cell and spatial transcriptomes with CytoSPACE. *Nat Biotech* 2023;**41**:1543–8. https://doi.org/10.1038/s41587-023-01697-9
Walker LA, Sovic MG, Chiang C-L *et al.* CLEAR: coverage-based limiting-cell experiment analysis for RNA-seq. *J Transl Med* 2020;**18**:63–15.
Wang D, Zhao C, Gao L *et al.* NPNT promotes early-stage bone metastases in breast cancer by regulation of the osteogenic niche. *J Bone Oncol* 2018a;**13**:91–6.
Wang X, Allen WE, Wright MA *et al.* Three-dimensional intact-tissue sequencing of single-cell transcriptional states. *Science* 2018b;**36**: 6400. https://doi.org/10.1126/science.aat5691
Weinhold N, Jacobsen A, Schultz N *et al.* Genome-wide analysis of non-coding regulatory mutations in cancer. *Nat Genet* 2014;**46**:1160–5.
Wolf FA, Angerer P, Theis FJ. SCANPY: large-scale single-cell gene expression data analysis. *Genome Biol* 2018;**19**:15.
Woodfield GW, Horan AD, Chen Y *et al.* TFAP2C controls hormone response in breast cancer cells through multiple pathways of estrogen signaling. *Cancer Res* 2007;**67**:8439–43.
Wu SZ, Al-Eryani G, Roden DL *et al.* A single-cell and spatially resolved atlas of human breast cancers. *Nat Genet* 2021;**53**:1334–47. https://doi.org/10.1038/s41588-021-00911-1
Xu H, Wang S, Fang M *et al.* SPACEL: deep learning-based characterization of spatial transcriptome architectures. *Nat Commun* 2023; **14**:7603. https://doi.org/10.1038/s41467-023-43220-3
Xu H, Zhao X-L, Liu X *et al.* Elevated ASCL2 expression in breast cancer is associated with the poor prognosis of patients. *Am J Cancer Res* 2017;**7**:955–61.
Yao Z, van Velthoven CTJ, Nguyen TN *et al.* A taxonomy of transcriptomic cell types across the isocortex and hippocampal formation. *Cell* 2021;**184**:3222–41.e26. https://doi.org/10.1016/j.cell.2021.04.021
Zhang B, He P, Lawrence JEG *et al.* A human embryonic limb cell atlas resolved in space and time. *Nature* 2024;**635**:668–78.
Zhou Z, Zhong Y, Zhang Z *et al.* Spatial transcriptomics deconvolution at single-cell resolution using Redeconve. *Nat Commun* 2023; **14**:7930. https://doi.org/10.1038/s41467-023-43600-9
Zoppino FCM, Guerrero-Gimenez ME, Castro GN *et al.* Comprehensive transcriptomic analysis of heat shock proteins in the molecular subtypes of human breast cancer. *BMC Cancer* 2018; **18**:700–17.


Bioinformatics, 2025, 41, 1–13
https://doi.org/10.1093/bioinformatics/btaf451
Original Paper